High Aspect Ratio Galfenol Flakes for High Strain Efficiency and Sensing Performance of Magnetostrictive Polymer Composites

Andrew D. M. Charles[ab]*, Andrew N. Rider[a], Sonya A. Brown[b] and Chun-Hui Wang[b]

[a] Defence Science and Technology Group, 506 Lorimer Street, Fisherman's Bend, VIC, Australia, 3207
[b] School of Mechanical and Manufacturing Engineering, University of New South Wales, Sydney, NSW, Australia, 2052.

*Corresponding author at Defence Science and Technology Group, 506 Lorimer Street, Fisherman's Bend, VIC, Australia, 3207 (Andrew D. M. Charles),
E: andrew.charles1@defence.gov.au, P: +61 3 9626 7263, F: +61 3 9626 7174

S1. Particle image processing

Particle geometry was determined via cross-sectioning and polishing of produced samples. Once polished, optical microscopy of the surface was performed, with image analysis via ImageJ. Images were first converted to binary, and colour thresholding used to outline the particles in the image, and ellipsoid shapes were fit to each of the particles using inbuild ImageJ macros. By assuming this ellipsoid shape, thickness and length measurements could be processed for all samples, with calculations of aspect ratio and approximate particle volume (assuming oblate ellipsoidal geometry for all particles) could be calculated. An example of the processing outputs from each of the analysis steps is shown in Figure S1.
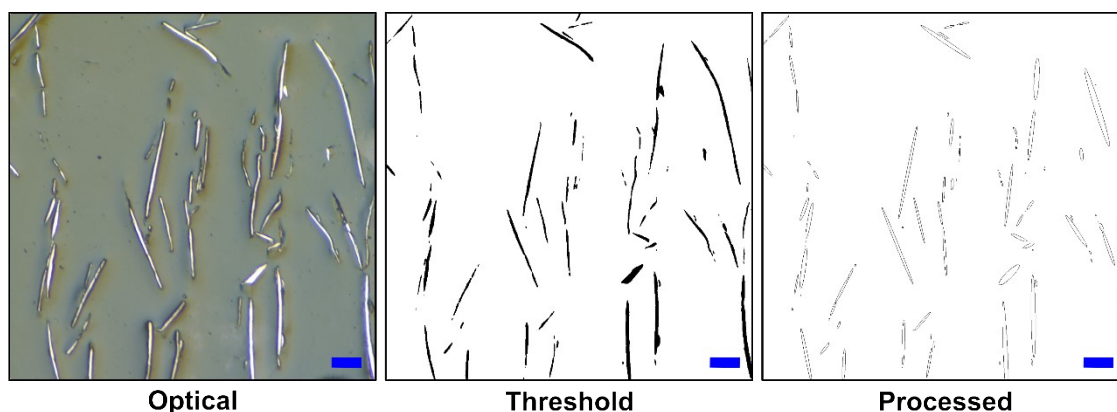

Optical   **Threshold**   **Processed**

Figure S1 Example of analysis steps undertaken to extract particle geometry data from optical microscopy images. Scale bars in each image represent 100 μm.

S2. Numerical Modelling Methodology

All numerical modelling was conducted using COMSOL® 5.6, with model geometry and physics generation performed in MATLAB, connected to COMSOL via MATLAB LiveLink™. Particle geometry information (aspect ratio mean and standard deviation, SD, alignment angle mean and SD, number of particles and particle volume fraction) were specified via MATLAB, with a script used to generate and distribute particles within a defined geometry based on this. Particle-particle interference and unit cell boundary interference checks were performed on all particles during generation until the required number of particles were generated within the unit cell. From here, analysis constraints,

boundary conditions, material properties and physics were defined to respective points, edges and domains in the model and the model generated in COMSOL via MATLAB LiveLink™. Due to automation of this process via a MATLAB script, variations in the model geometry could be easily implemented and numerous iterations performed. A minimum of 40 models were run for each geometric variation, with statistical analysis of the results performed using the MATLAB Statistics and Machine Learning Toolbox. The workflow of this modelling approach as applied to the multi-particle model is shown in Figure S2.

The electromagnetics and structural mechanics modules were implemented for physics definitions in COMSOL. Within the structural mechanics physics, a linear elastic material definition was assumed for the polymer matrix, whilst the magnetostrictive material definition was applied to the particles. Rigid motion suppression was used to constrain the polymer matrix unit cell, allowing all faces of the cell to move in response to the applied magnetic field and subsequent particle strain. A uniform background magnetic flux density was used to represent the applied field to the unit cell, with an external magnetic vector potential boundary condition implemented to the external air boundaries to force the total applied field to be equal to the background field (reduced magnetic vector potential at the boundaries was thus zero). Due to the highly non-linear nature of the magnetic fields in the model (on account of the particulates), difficulty in attaining convergence was overcome through the addition of linear discretization and A-field gauge fixing to the model (implemented in the magnetic field module).
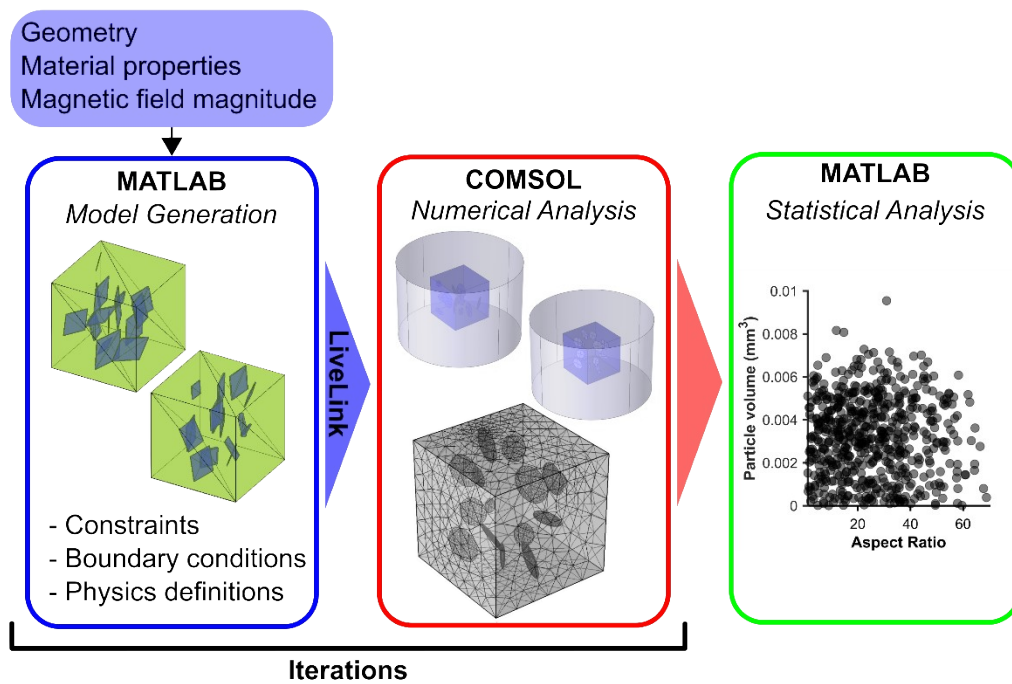

Figure S2 Example workflow utilised for the multi-particle numerical modelling

As a validation example, the effect of aspect ratio on the internal field strength was computed for a prolate and oblate spheroids, and compared to the analytical solutions presented in [28]. Particles were of a fixed volume of 1×10^{-9} m^3 and magnetic permeability, μ_r, of 100, with the long-axis being parallel and perpendicular to a uniform 1.0 A/m magnetic field. Results are shown in Figure S3.
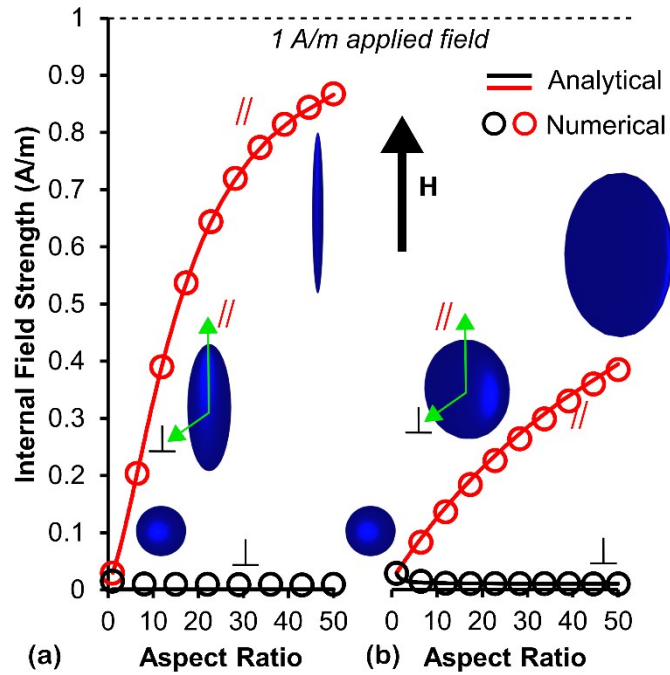
Figure S3 Internal field strength as a function of aspect ratio for (a) prolate (rod-like) and (b) oblate spheroid (flake-like) geometries (volume of $1x10^{-9}$ m^3) subject to a uniform 1 A/m applied magnetic field. Solid lines show analytical results [28] whilst open marker points show numerically calculated results.

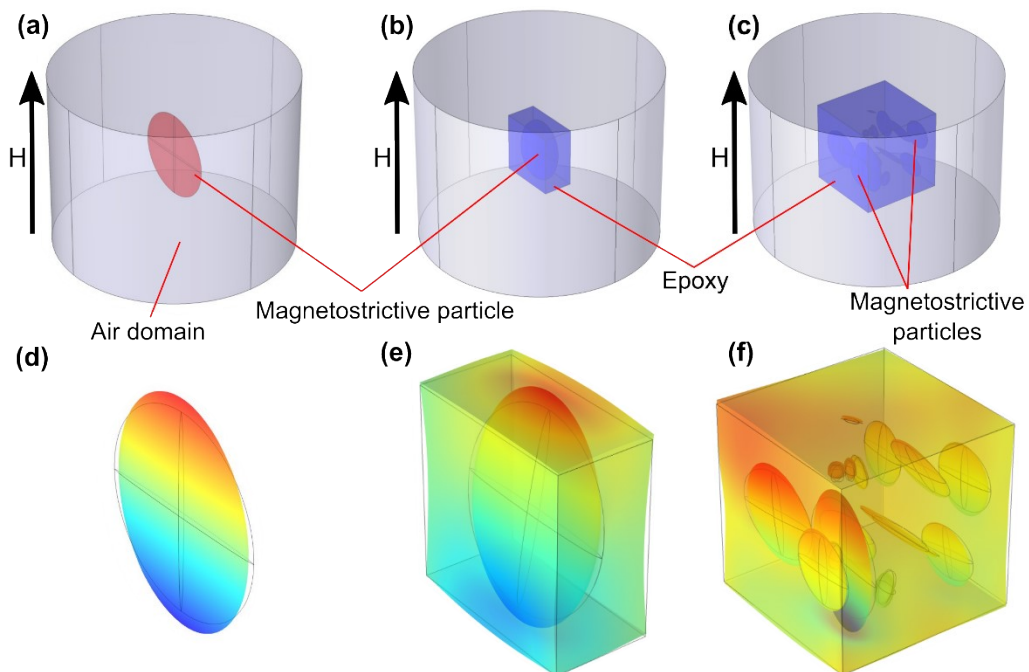Examples of the three model types utilised in the study are shown in Figure S4.

Figure S4 Models utilised: (a) shows the single particle model with no matrix, (b) the single particle RVE and (c) the multi-particle RVE model, with example displacement fields (in the applied H direction) shown in (d), (e) and (f), respectively.

S3. Statistical analysis of modelled results

For all geometry changes to the multi-particle numerical model, a minimum of 40 model iterations were performed to form a reasonable distribution of particle shapes to reflect the desired geometry input. Typically, 15 particles were considered in each unit cell, thus amounting to 600 particles (over the 40 iterations) modelled for each geometry case. In each geometry case, normal probability plots and histograms of the aspect ratio provided a gauge of the aspect ratio and particle volume distributions. As an example, Figure S5 shows the normal probability plots for a very small aspect ratio SD (0.1) at two different angular alignment SD's, 0° and 10°. As can be observed, excellent fit to the normal distribution is achieved at this low SD, which is also reflected in the histogram and scatter plot results of Figures S6 and S7.
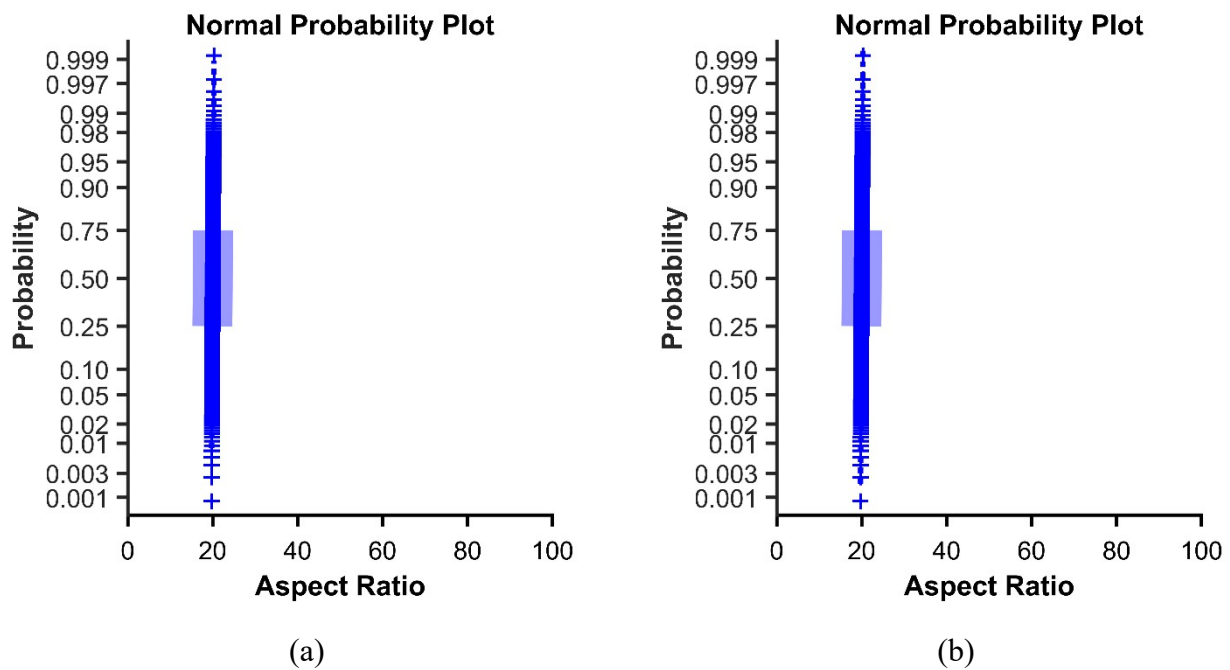

(a)   (b)

Figure S5 Normal probability plots for multi-particle model runs with aspect ratio mean of 20 and SD of 0.1; (a) shows the results for perfect particle angular alignment (alignment standard deviation of 0°) whilst (b) shows a particle alignment standard deviation of 10°.
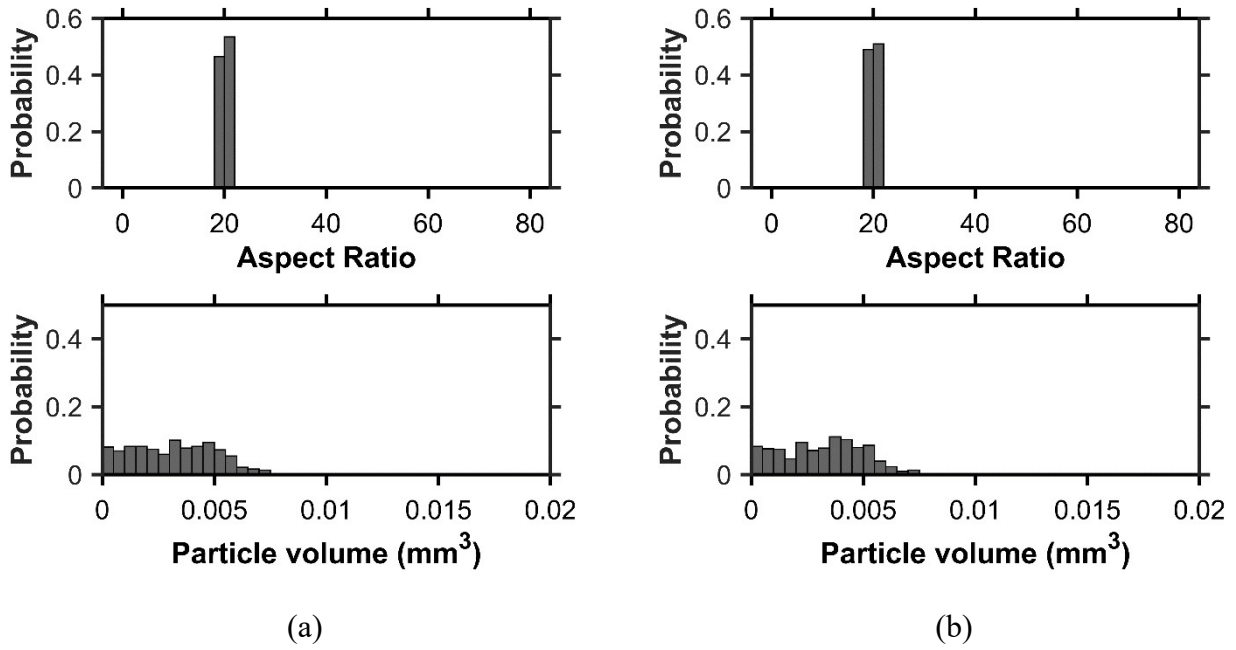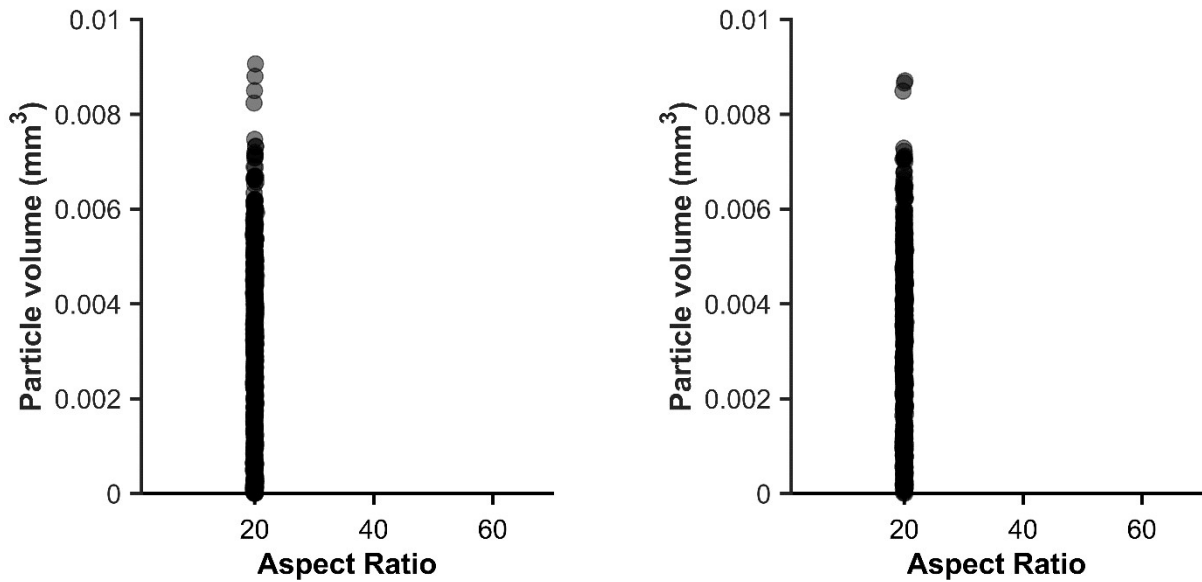
Figure S6 Histograms of aspect ratio and particle volume for multi-particle model runs with an aspect ratio mean of 20 and standard deviation of 0.1; (a) shows the results for perfect particle angular alignment (alignment standard deviation of 0°) whilst (b) shows a particle alignment standard deviation of 10°.

Figure S7 Particle volume vs. aspect ratio for all particles analysed using the multi-particle model with an aspect ratio mean of 20 and standard deviation of 0.1; (a) shows the results for perfect particle angular alignment (alignment standard deviation of 0°) whilst (b) shows a particle alignment standard deviation of 10°.

The inclusion of a broader SD to the aspect ratio results in a tilting of the normal probability plot and a slight deviation from the normal distribution at the lower aspect ratios, as can be seen in the results of Figure S8. This deviation at low aspect ratio is on account of the particle generation methodology, which logically prevents the formation of particles with aspect ratios less than 1 (a sphere). Further, a slight light-tailedness is observed at the higher aspect ratios, seen as a drop in the particle occurrence probability below the expected normal trend, and by the histogram results of Figure S9. This is again is on account of the particle generation methodology in which particle-particle conflict and particle-boundary conflicts should result in preferential selection of lower aspect ratio particles in order to fit the particles within the unit cell at a defined volume fraction. This is particularly the case when angular mis-alignment is incorporated. Despite this, only a slight deviation is observed from the normal distribution at these higher aspect ratios, and this is believed to be offset by a reduction in volume for these higher aspect ratio particles, as seen by the slight skewness in the volume distribution observed in Figure S10.
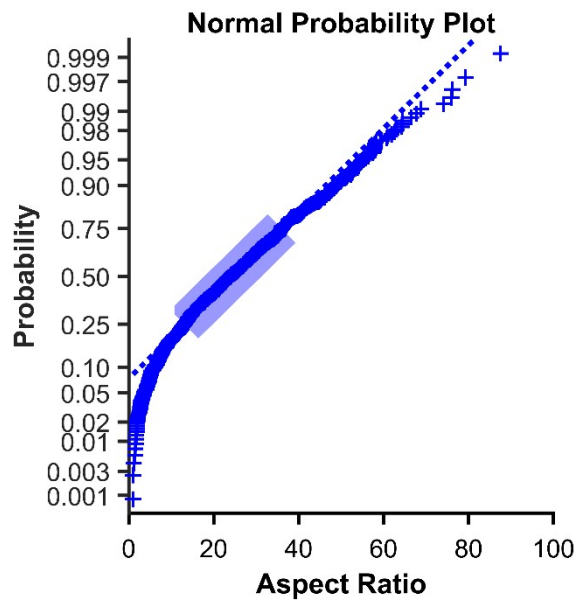

Figure S8 Normal probability plot for multi-particle model runs with an aspect ratio mean of 20, aspect ratio standard deviation of 20 and alignment standard deviation of 20°.
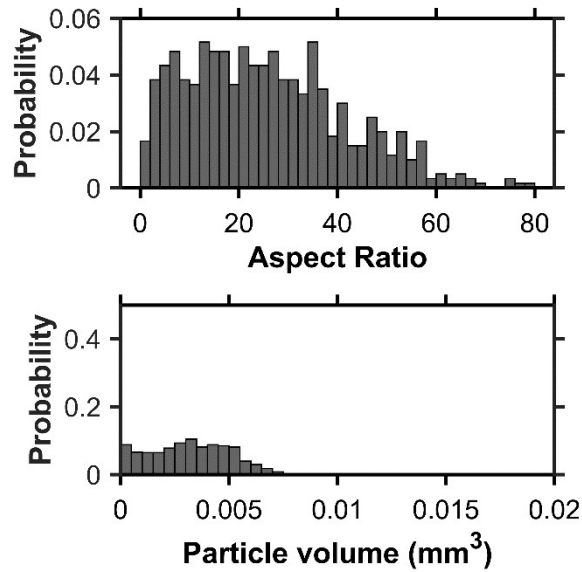
Figure S9 Histogram of Aspect ratio and particle volume for multi-particle model runs with an aspect ratio mean of 20, aspect ratio standard deviation of 20 and alignment standard deviation of 20°.
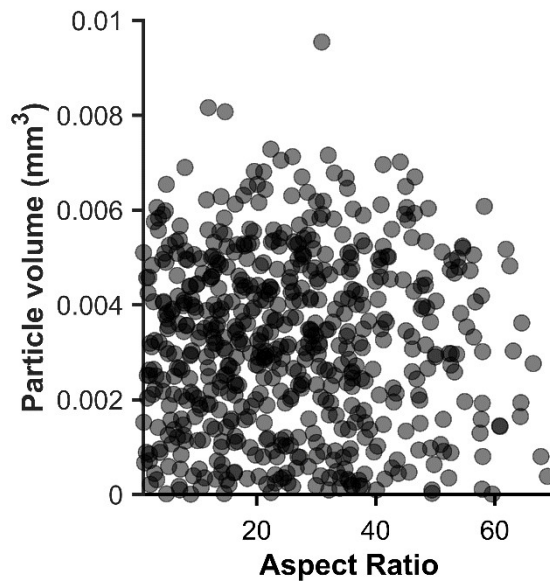

Figure S10 Particle volume vs. aspect ratio for all particles analysed using the multi-particle model with an aspect ratio mean of 20, aspect ratio standard deviation of 20 and alignment standard deviation of 20°.

S4. Volume resistivity measurement

Volume resistivity in the particle alignment direction for a number of different samples was measured using load cell monitored copper electrodes connected to an Electrometer (Keysight technologies, USA). A load of 50 N was applied during measurement, with a minimum of three samples tested for each coupon type. Theoretical percolation behaviour based on the normalised percolation theory [1] was used to interpret the results. This theory describes the composite conductivity, σ, as

$$\sigma = \sigma_c + (\sigma_m - \sigma_c)\left(\frac{\varphi - \varphi_c}{F - \varphi_c}\right)^t \tag{S1}$$

where σ_c is the conductivity at percolation, σ_m is the maximum conductivity, φ is the volume concentration, φ_c the critical volume concentration at percolation, F is the packing factor and t is a universal exponent which describes the increase in conductivity above percolation.
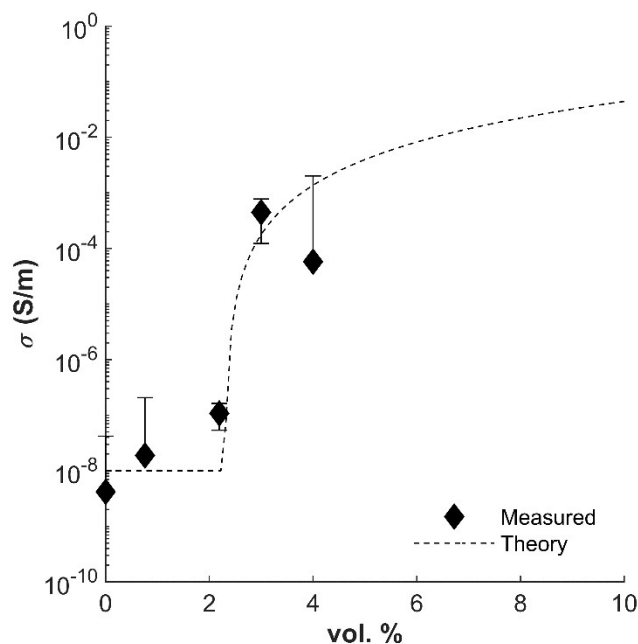

Figure S11 Volumetric conductivity vs. Galfenol volume fraction for 3 hour milled and magnetically aligned samples. Error bars show standard deviation in three samples measured.

Figure S11 shows the experimental volume conductivity results as compared to the theoretical model fit established via Equation S1. Measurements were made in the flake alignment direction, with results for the 3 hour milled Galfenol shown. For the fit, F was assumed to be 0.2 based on [2], whilst a value of 2.3 was utilised for t.

S5. High energy X-ray diffraction

For diffracted signal collection, a Mythen II microstrip detector (DECTRIS, Baden-Dattwil, Switzerland) was used over the range of $10° \le 2\theta \le 89°$ in flat-plate asymmetric reflection geometry, whilst the sample was rotated in a capillary spinner.

Figure S13 shows the set-up utilised to apply varying magnetic fields to the samples whilst recording X-Ray diffraction data at the Australian Synchrotron. A Neodymium magnet was shifted relative to the analysis region on the capillary holding the sample under investigation. Prior to XRD analysis, the field strength parallel to the length of the capillary created by the magnet was measured at varying offsets in order to correlate XRD results with an applied field, these field strength values are shown in Figure S13.
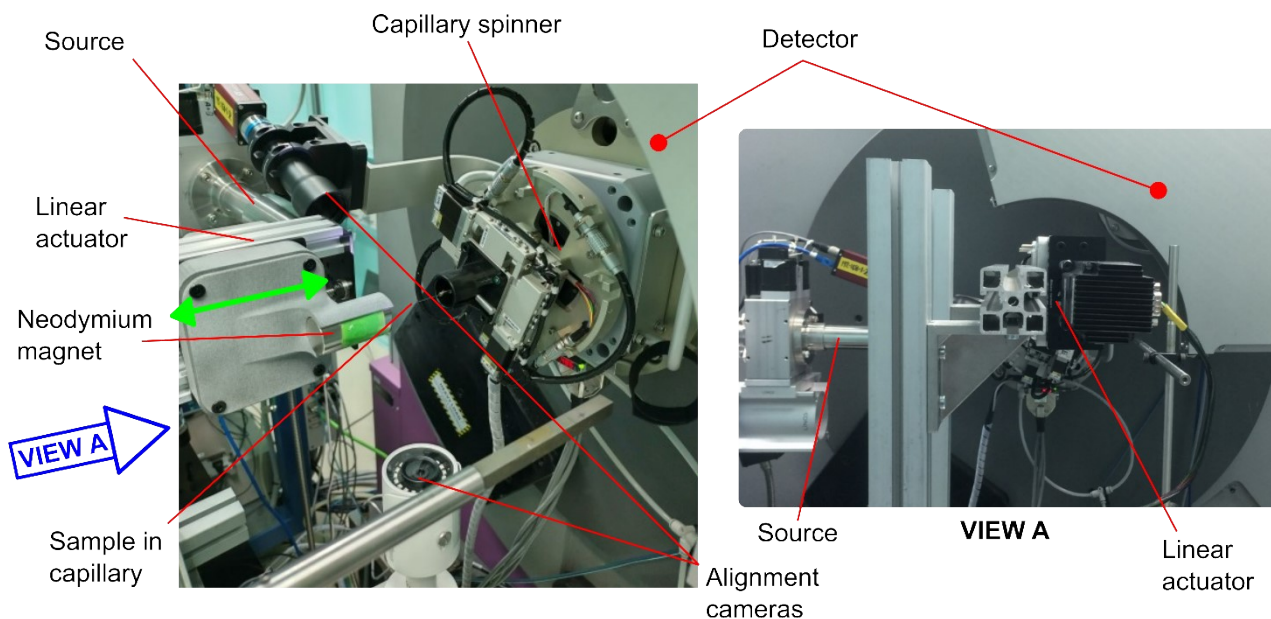
Figure S12 Set-up used to obtain high energy XRD data from the composite samples whilst varying an in-situ applied magnetic field.
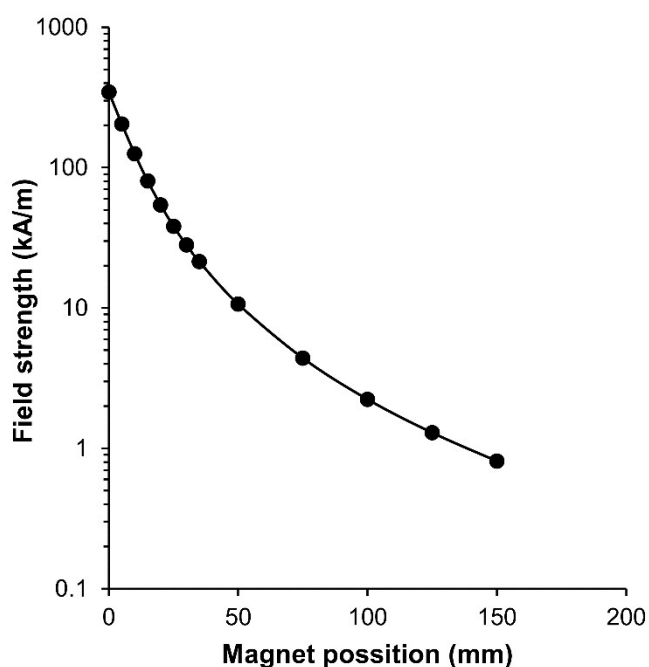

Figure S13 Measured field strength of Neodymium magnet at various offset positions.

S6. Rietveld refinement of crystal structure

Rietveld refinement was used to fit the galfenol crystal structure to the obtained Synchrotron XRD data. Prior to running all samples, a National Institute of Standards and Technology (NIST) Standard Reference Material (SRM) was processed and refined in order to establish instrument corrections, zero error and wavelength. In this instance, an SRM 660b was used, consisting of approximately 6 g of lanthanum hexaboride, LaB_6, powder bottled under argon. Subsequent sample testing was then performed on different sample mill times and under different applied magnetic fields. All samples

were measured in 0.7 mm quartz capillaries, with Galfenol powders combined with epoxy and injected into the capillaries using syringes, followed by magnetic alignment during cure. For refinement, a 20 term Chebyshev polynomial background was assumed and refinement performed over a 10° - 80° range. Examples of the acquired and refined XRD profiles for 0, 1 and 8 hours of high energy ball milling are shown in Figures S14 to S16 respectively.
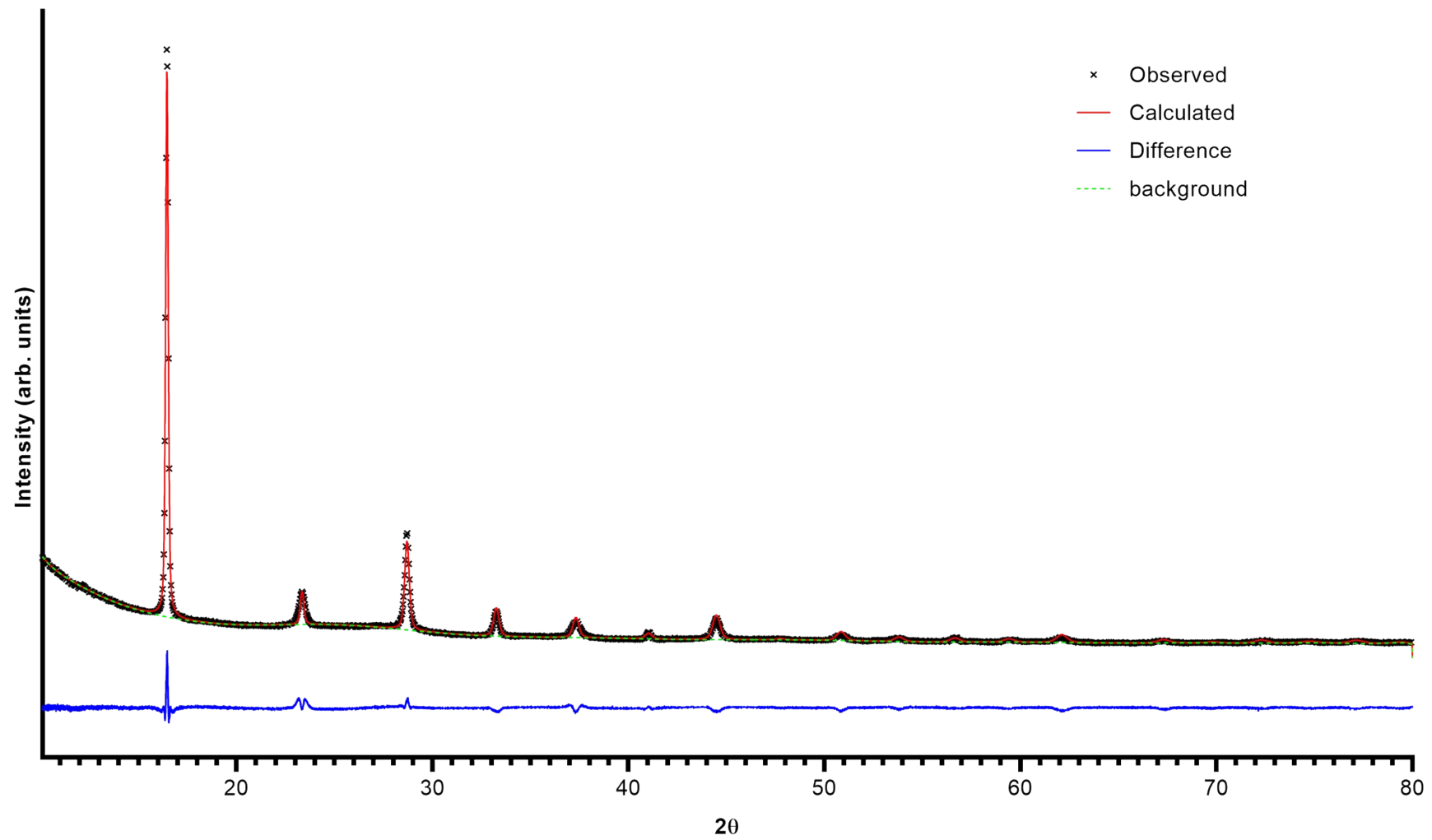
Figure S14 Measured (observed) and refined (calculated) XRD profiles for the 0 hour high energy ball milled galfenol sample.
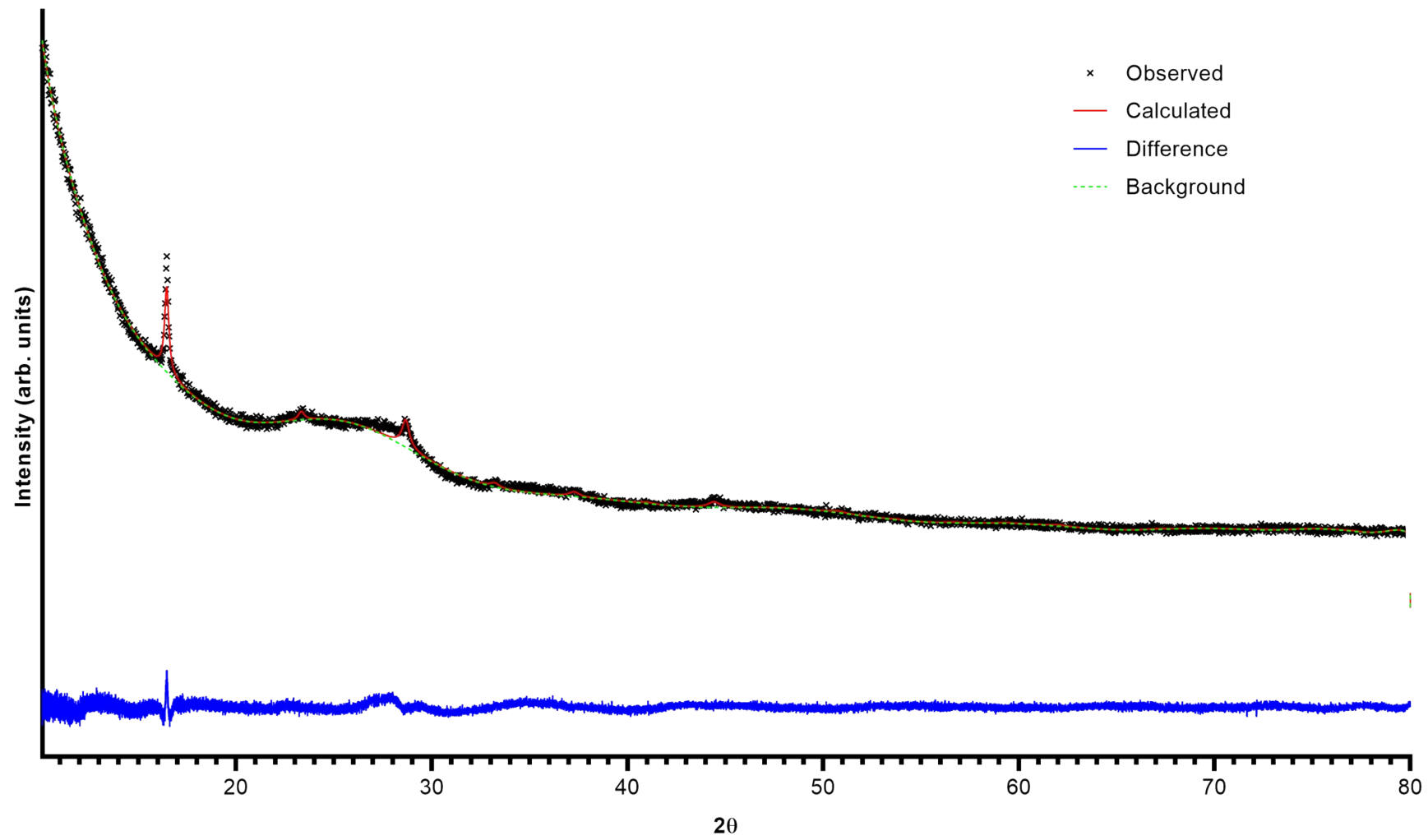
Figure S15 Measured (observed) and refined (calculated) XRD profiles for the 1 hour high energy ball milled galfenol sample.
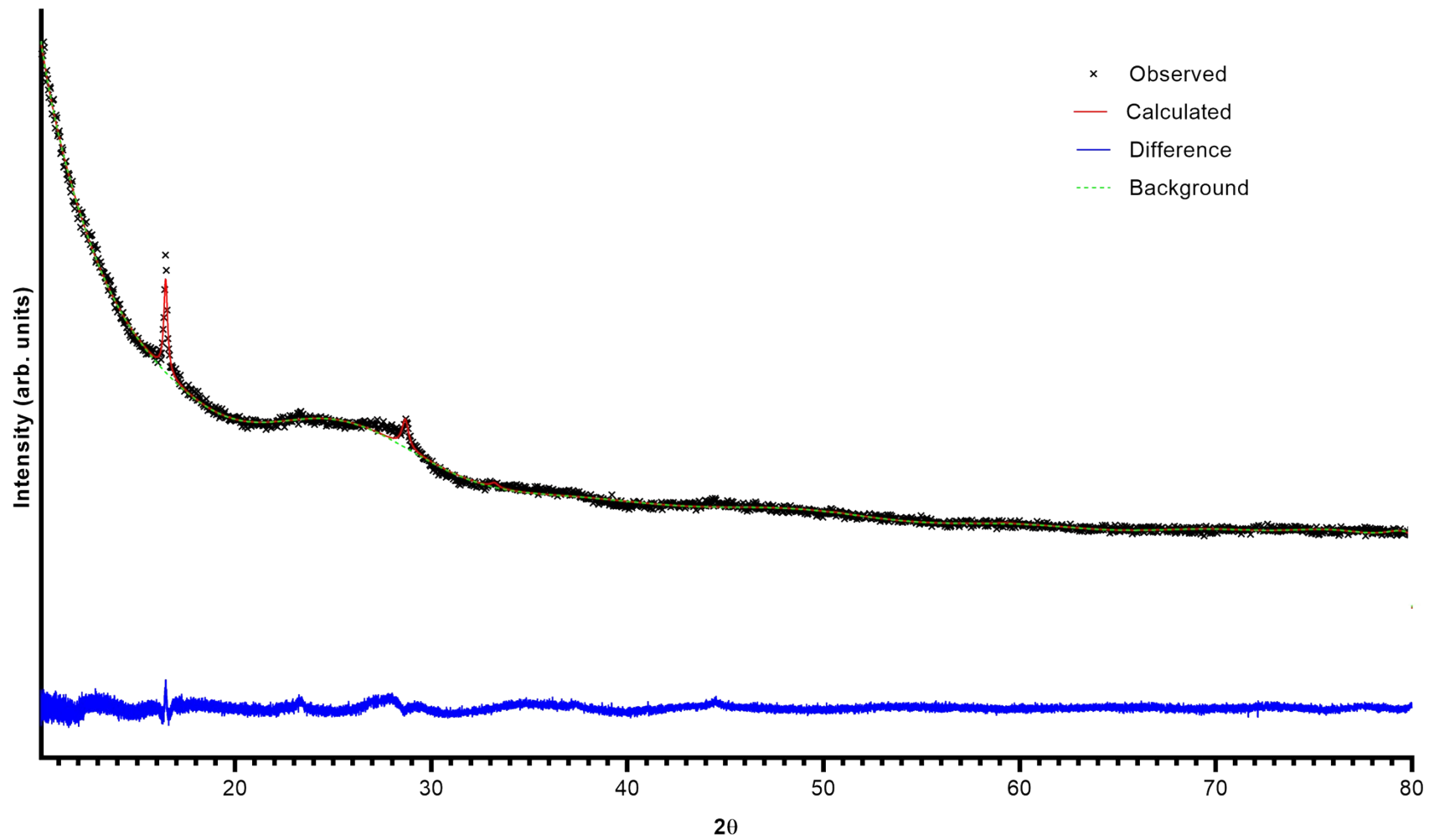
Figure S16 Measured (observed) and refined (calculated) XRD profiles for the 8 hour high energy ball milled galfenol sample.

S7. Dynamic Mechanical Thermal Analysis

Dynamic Mechanical Thermal Analysis (DMTA) results of the composite and neat epoxy systems as a function of temperature for four heating cycles are presented in Figures S17 and S18 for the neat epoxy and composite systems respectively.
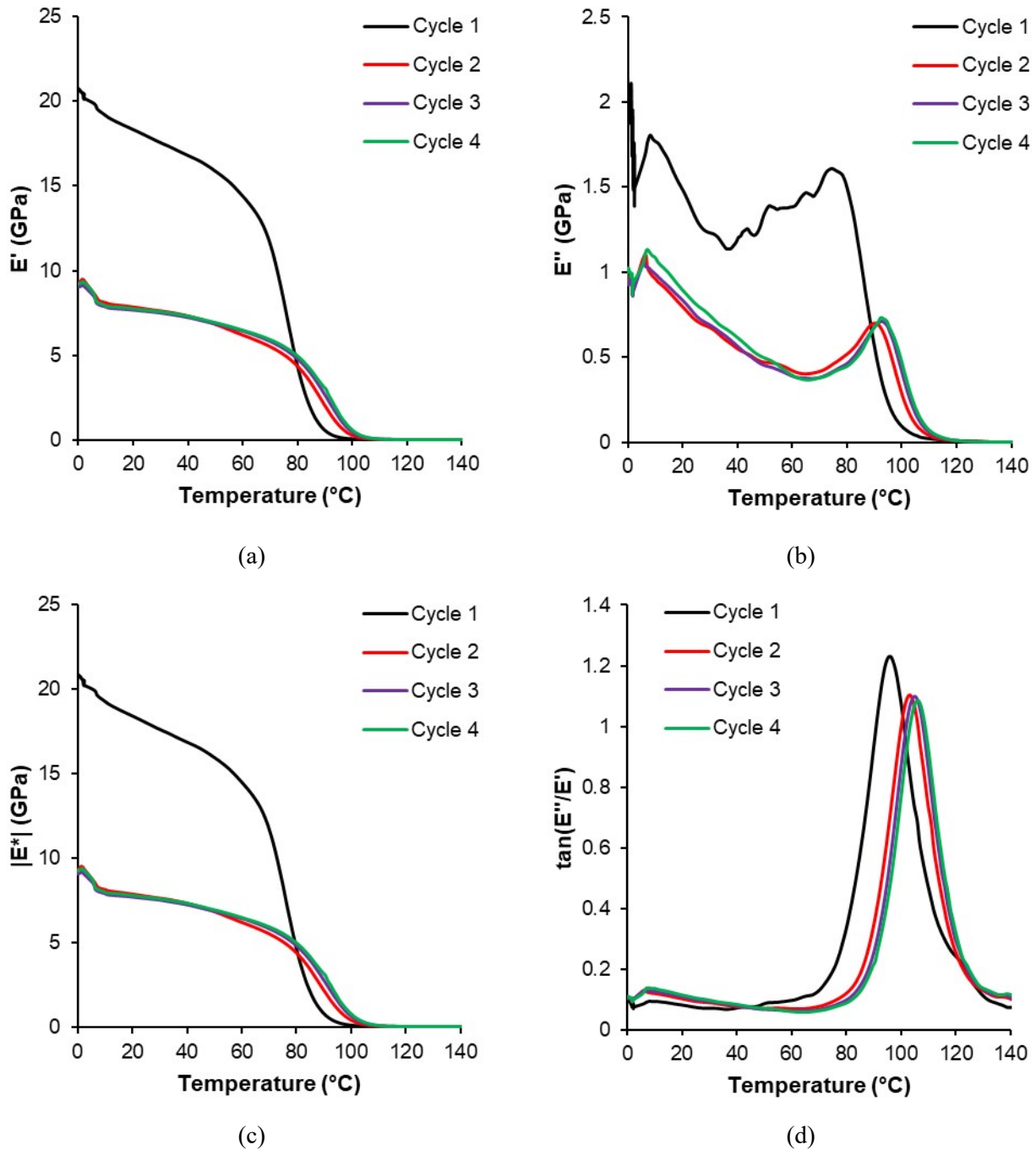

(a)

(b)

(c)

(d)

Figure S17 DMTA results for the neat epoxy system as a function of temperature for four heating cycles: (a) Storage modulus, (b) loss modulus, (c) complex modulus and (d) tan(E"/E').
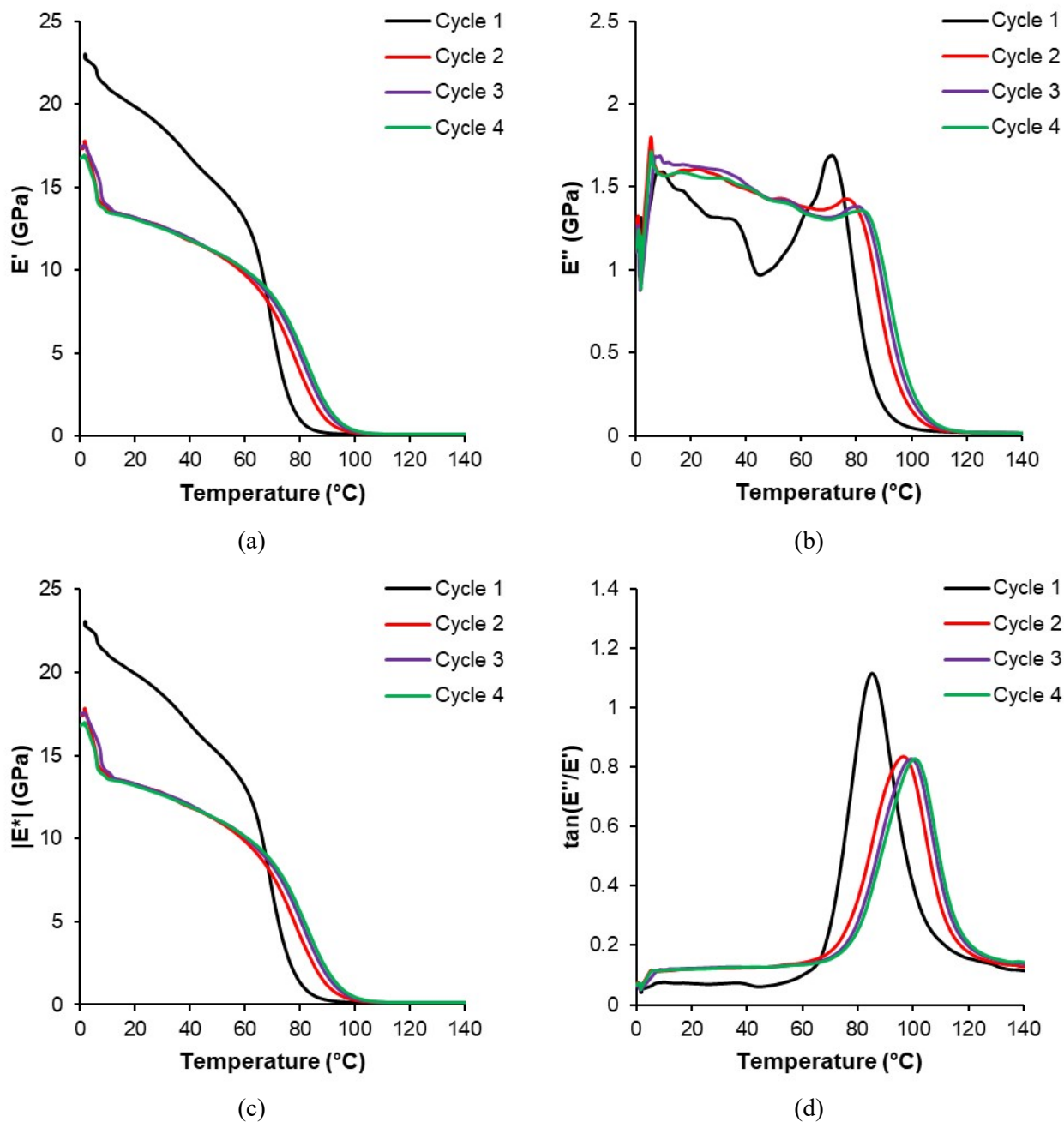
(a)

(b)

(c)

(d)

Figure S18 DMTA results for a 2.64 vol. % composite as a function of temperature for four heating cycles: (a) Storage modulus, (b) loss modulus, (c) complex modulus and (d) tan(E''/E').

References

[1]   Lebedev EV, Mamunya Y, Shut MI, Muzychenko Y, Pissis P. Percolation phenomena in polymers containing dispersed iron. Polym Eng Sci 2002;42:90–100. https://doi.org/10.1002/pen.10930.

[2]   Yellampalli S. Carbon Nanotubes: Polymer Nanocomposites. BoD – Books on Demand; 2011.